

Nonstoichiometric Titanium Oxides via Pulsed Laser Ablation in Water

Chang-Ning Huang · Jong-Shing Bow ·
Yuyuan Zheng · Shuei-Yuan Chen ·
New Jin Ho · Pouyan Shen

Received: 10 January 2010 / Accepted: 27 March 2010 / Published online: 13 April 2010
© The Author(s) 2010. This article is published with open access at Springerlink.com

Abstract Titanium oxide compounds TiO , Ti_2O_3 , and TiO_2 with a considerable extent of nonstoichiometry were fabricated by pulsed laser ablation in water and characterized by X-ray/electron diffraction, X-ray photoelectron spectroscopy and electron energy loss spectroscopy. The titanium oxides were found to occur as nanoparticle aggregates with a predominant 3+ charge and amorphous microtubes when fabricated under an average power density of ca. $1 \times 10^8 \text{ W/cm}^2$ and 10^{11} W/cm^2 , respectively followed by dwelling in water. The crystalline colloidal particles have a relatively high content of Ti^{2+} and hence a lower minimum band gap of 3.4 eV in comparison with 5.2 eV for the amorphous state. The protonation on both crystalline and amorphous phase caused defects, mainly titanium rather than oxygen vacancies and charge and/or volume-compensating defects. The hydrophilic nature and presumably varied extent of undercoordination at the free surface of the amorphous lamellae accounts for their rolling as tubes at water/air and water/glass interfaces. The nonstoichiometric titania thus fabricated have potential optoelectronic and catalytic applications in UV-visible

range and shed light on the Ti charge and phase behavior of titania-water binary in natural shock occurrence.

Keywords Titanium oxide · Nonstoichiometry · Structure · Optical property · Pulsed laser ablation in water · TEM

Introduction

Nanobelts of semiconducting oxides of zinc, tin, indium, cadmium, and gallium were discovered by simply evaporating the desired commercial metal oxide powders at high temperatures [1]. Such nanobelts shed light on a distinctive and common structural characteristic for the family of semiconducting oxides with cations of different valence states and materials of distinct crystallographic structures. The nanobelts were also suggested to be an ideal system for fully understanding dimensionally confined transport phenomena in functional oxides and building functional devices along individual nanobelts [1]. Since then, nano-size and one-dimensional semiconductor oxide nanomaterials, such as zincite (ZnO) nanocrystals with Mn dopant to modify the UV emission [2] and titania (TiO_2) polymorphs with many applications [3], have received intensive interests regarding their synthesis and applications on novel optical, photoelectricity, catalysis, and piezoelectricity properties. (The titanium oxide polymorphs have particularly attracted research community on their unique physical and chemical properties and wide applications such as paints, plastics, papers, coatings, cosmetics, ceramics, electronics, and photo-catalysts [3].) A hydrothermal route in the presence of stabilizer and/or acids was commonly adopted for the synthesis of titanium oxide phases with specific crystal structure and novel shape, such as TiO_2

C.-N. Huang · Y. Zheng · N. J. Ho · P. Shen (✉)
Center for Nanoscience and Nanotechnology, National Sun
Yat-sen University, Kaohsiung, Taiwan, Republic of China
e-mail: pshen@mail.nsysu.edu.tw

C.-N. Huang · Y. Zheng · N. J. Ho · P. Shen
Department of Materials and Optoelectronic Science, National
Sun Yat-sen University, Kaohsiung, Taiwan, Republic of China

J.-S. Bow
E. B. Tech Co., Ltd., Taipei, Taiwan, Republic of China

S.-Y. Chen
Department of Mechanical and Automation Engineering, I-Shou
University, Kaohsiung, Taiwan, Republic of China

rutile nanoparticles [4], anatase nanotubes [5], and tubular titanium hydrates with controversial stoichiometries and structures [6–10]. In general, the tailoring of phase structure, particle morphology and hence the properties of the titanium oxides by this wet route were attributed to the precursor used, the presence of anionic species and the pH of the solution which affect the nucleation/growth processes.

Here, we used an alternative route of pulsed laser ablation in liquid (PLAL) to synthesize nonstoichiometric TiO_x nanoparticles and nanotubes in a subsequent water-driven assembly process. This stabilizer-free approach is quite different from surfactant/copolymers or other template-assisted assembly of TiO_x nanoparticles in a desired manner. The synthesis of such a tubular material from atom clusters and their lamellar derivative is analogous to the fabrication of carbon onions via arc discharge in water [11] and Au tubes via PLAL and subsequent dwelling in water [12]. We focused on the nonstoichiometry, shape, coalescence, and dense structure, if any, of the TiO_x nanocondensates and the phase behavior upon electron irradiation as of concern to the space charge, the surface/interface energetics in terms of unrelaxed or relaxed state and theoretical band gap of such metastable phases [13, 14] for potential optoelectronic applications.

Experimental Section

PLAL Synthesis of TiO_x Nanocondensates

To produce TiO_x nanocondensates, Ti (99.99% pure, 1.0 mm in thickness) plate immersed in de-ionized water within a glass beaker was subjected to energetic Nd-YAG-laser (Lotis, 1064 nm in wavelength, beam mode: TEM00)

pulse irradiation for up to 3000 pulses inside an ablation chamber under the laser parameters compiled in Table 1. A relatively high power density of $1.4 \times 10^{11} \text{ W/cm}^2$ (i.e. pulsed energy 650 mJ/pulse; pulse duration 16 ns; beam size 0.03 mm^2 ; fluence 2.2 kJ/cm^2 ; frequency 10 Hz under Q-switch mode) caused a larger yield of atom clusters as a colloidal solution. The solution was then settled in capped vial for up to one week in desiccators in order to study the assembly of the resultant multiple walled tubes (MWTs).

Characterization

The optical absorbance of the as-deposited nanocondensates and further developed MWTs in solution with specified dwelling times were acquired by a UV–Vis spectrophotometer (U-3900H, Hitachi) operating at an instrumental resolution of 0.1 nm in the range of 200 to 800 nm. The powders recovered from such samples were dried for microstructure observations using optical polarized microscopy and scanning electron microscopy (SEM, JEOL JSM-6700F, 10 kV, $10\mu\text{A}$). The crystal structure of the MWTs was determined by X-ray diffraction (XRD, Bede D1, Cu K α , 40 kV, 30 mA, at 0.05° and 3 s per step from 2θ angle for 20° up to 100°). The d-spacings measured from XRD trace were used for least-squares refinement of the lattice parameters with an error $\pm 0.0001 \text{ nm}$ using bulk gold reflections as a standard.

Field emission scanning transmission electron microscopy (STEM, FEI Tecnai G2 F20 at 200 kV) with selected area electron diffraction (SAED), and point-count energy dispersive X-ray (EDX) analysis at a beam size of 1 nm was used to study the structure and composition of the nanoparticles and the tubular walls. Z-contrast images and compositional line scanning profiles are acquired by high-angle annular dark-field (HAADF) detector and EDX under

Table 1 Laser ablation parameters and resultant phase assemblages of nonstoichiometric titanium oxides via PLAL

| Sample number | 1 | 2 | 3 | 4 |
|---|------------|------------|-------------------|-------------------|
| 1064 nm excitation | FR | FR | QS | QS |
| Pulsed energy (mJ/pulse) | 900 | 1100 | 550 | 650 |
| Pulse duration | 0.24 ms | 0.24 ms | 16 ns | 16 ns |
| Beam size (mm^2) | 0.03 | 0.03 | 0.03 | 0.03 |
| Fluence (kJ/cm^2) | 3.0 | 3.7 | 1.8 | 2.2 |
| Frequency (Hz) | 10 | 10 | 10 | 10 |
| Power density (10^7 W/cm^2) | 13 | 15 | 1.1×10^4 | 1.4×10^4 |
| Phases | A < T1T2T3 | A < T1T2T3 | A > T1T2T3 | A > T3 |
| Assembly | NCA | NCA | MWT | MWT |
| Internal stress (GPa)* | 5.2 | 5.5 | 4.2 | 4.5 |

FR free run mode, QS Q-switch mode, A amorphous phase, T1 TiO , T2 Ti_2O_3 , T3 TiO_2 , NCA nano chain aggregate, MWT multiple wall tube

* Based on SAED lattice parameter of the TiO_2 nanocondensates and the Birch-Murnaghan equation of state of the rutile with relevant bulk modulus and its pressure derivative [45] (cf. text)

STEM mode. Lattice imaging coupled with Fourier transform patterns were used to study the rolling planes of the MWT and their partial epitaxy relationship with the associated TiO_x nanoparticles. The Gatan Image Filter (GIF) coupled with electron energy loss spectrum (EELS) by TEM was employed to identify the chemical bonding state of the individual TiO_x nanoparticle and that associated with the nanotubes.

Powdery sample mixed with KBr was studied by FTIR (Bruker 66v/S) for the extent of OH^- signature on MWT. The powdery MWTs settled on a vitreous SiO_2 substrate were studied by micro-Raman in a backscattering geometry by a Jobin-Yvon HR800 system working in the triple-subtractive mode for the estimation of internal stress for the constituting TiO_6 and/or TiO_4 polyhedra. The same sample was also examined by X-ray photoelectron spectroscopy (XPS, JEOL JPS-9010MX, Mg $K\alpha$ X-ray source) calibrated with a standard of C 1 s at 284 eV for the determination of Ti^{2+} , Ti^{3+} , and Ti^{4+} peaks. Photoluminescence (PL) spectra of the powdery samples were recorded using a Jobin-Yvon spectrophotometer (Trix 320) at an excitation wavelength of 325 nm (He-Cd laser) at room temperature.

Results

Phase Identity and General Behavior of the Condensates upon Dwelling in Water

According to the combined XRD (Fig. 1) and electron microscopic evidences, the as-fabricated nanoparticles with an average particle size of ca. 20 nm are predominantly TiO , Ti_2O_3 , and TiO_2 rutile with a considerable extent of nonstoichiometry when fabricated by specified laser parameters denoted as 1, 2, 3, and 4 (cf. Table 1). The phases remained unchanged despite a much higher assembly/sedimentation rate for samples 3 and 4 than 1 and 2, the latter typically formed nano chain aggregate (NCA), upon dwelling in water for a week. The nanoparticles in all samples were more or less precipitated in the bottom of the vial in the first day of dwelling. After a week of dwelling in water, additional tubular materials with micron-scale diameter were deposited from samples 3 and 4, which were fabricated at a much higher power density than samples 1 and 2. The optical property, microstructure, and composition of the phases are shown representatively in the following.

UV–Visible Absorbance of the Colloidal Solutions

The colloidal titanium oxide solutions as formed via PLAL in free run mode (i.e. samples 1 and 2) are sky-blue, whereas those produced by a much higher power density

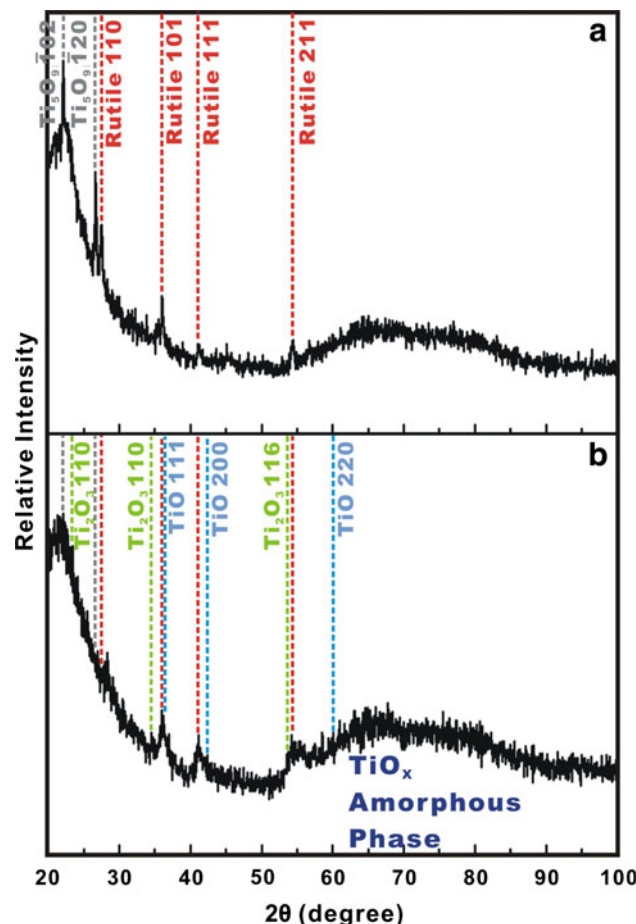


Fig. 1 XRD patterns (CuK_{α}) of partially crystallized titanium oxide nanocondensates: **a** sample 4 with predominant rutile and amorphous phase besides minor Ti_5O_9 , **b** sample 1 with nonstoichiometric TiO , Ti_2O_3 , Ti_5O_9 , and rutile besides the amorphous phase. The broad diffraction maximums below 30° and above 50° in 2θ are due to glass substrate and amorphous phase, respectively

under Q-switch mode (i.e. samples 3 and 4) are muddy-white under the naked eye (not shown). After dwelling in water for a week (Fig. 2a), more deposits were formed from the colloidal solutions of samples 3 and 4 than samples 1 and 2. The optical absorbance near UV region for samples 1 and 2 is basically similar to that of the TiO_2 nanocondensates in aqueous or solvent-protected solution [15, 16]. A slightly higher power density cause a higher concentration of the nanocondensates and hence a considerably higher absorbance for sample 2 than sample 1. Samples 3 and 4 prepared by a power density almost 3 orders-of-magnitude higher than samples 1 and 2 showed a significant absorbance peak near 200 nm. Sample 3 also showed an absorption shoulder similar to that of samples 1 and 2 presumably due to Ti^{2+} and Ti^{3+} ions, as discussed later. Room temperature aging of the solution for up to 1 week caused progressive accumulation of the opaque materials at the bottom and along the humidified wall of

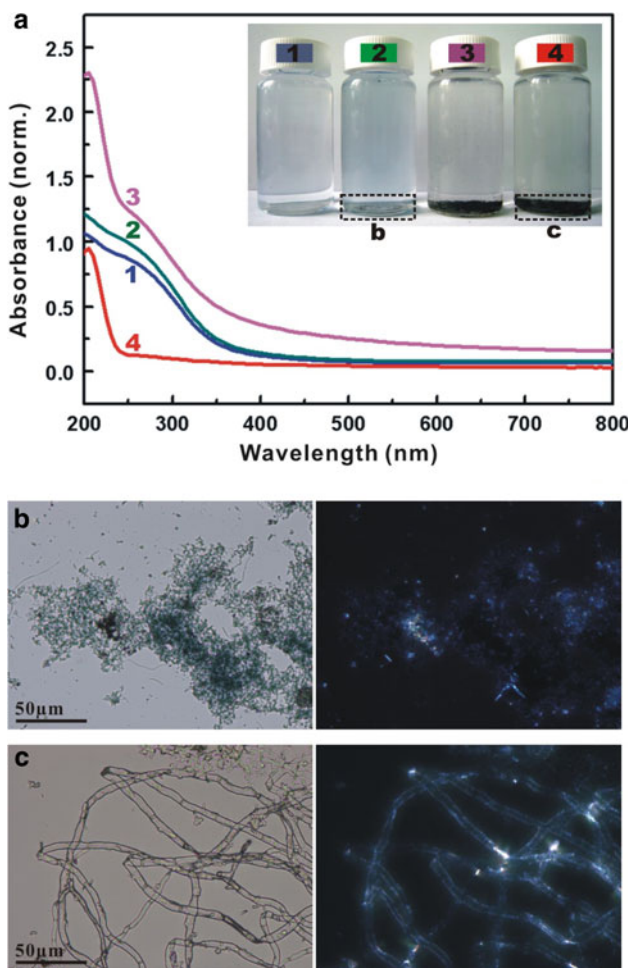


Fig. 2 **a** UV-visible absorption spectra and corresponding photos of colloidal titanium oxide solutions (inset) produced by PLAL under specified laser parameters 1 to 4 (cf. Table 1) and then settled for 1 week, showing broadened absorption below 400 nm for the samples 1 to 3 fabricated under relatively low power density, and sharp absorption below ca. 230 nm for sample 4 by the highest power density of $1.4 \times 10^{11} \text{ W/cm}^2$. **b** and **c** Optical micrographs under open polarizer (*left*) and crossed polarizers (*right*) for the deposit in samples 2 (*top panel*) and 4 (*bottom panel*) showing titanium oxide nanocondensates were assembled as particles and tubes, respectively

the capped bottle, and hence lowering of the absorbance peak, in particular sample 4.

Microscopic Observations of the Assembled Nanoparticles

Optical micrographs under open and crossed polarizers for the representative deposits retrieved from sample prepared under a relatively low (i.e. sample 2) and 3 orders-of-magnitude higher power density (i.e. sample 4) showed that the titanium oxides tended to assemble as particles in the former case (Fig. 2b) but tubes in the latter case (Fig. 2c).

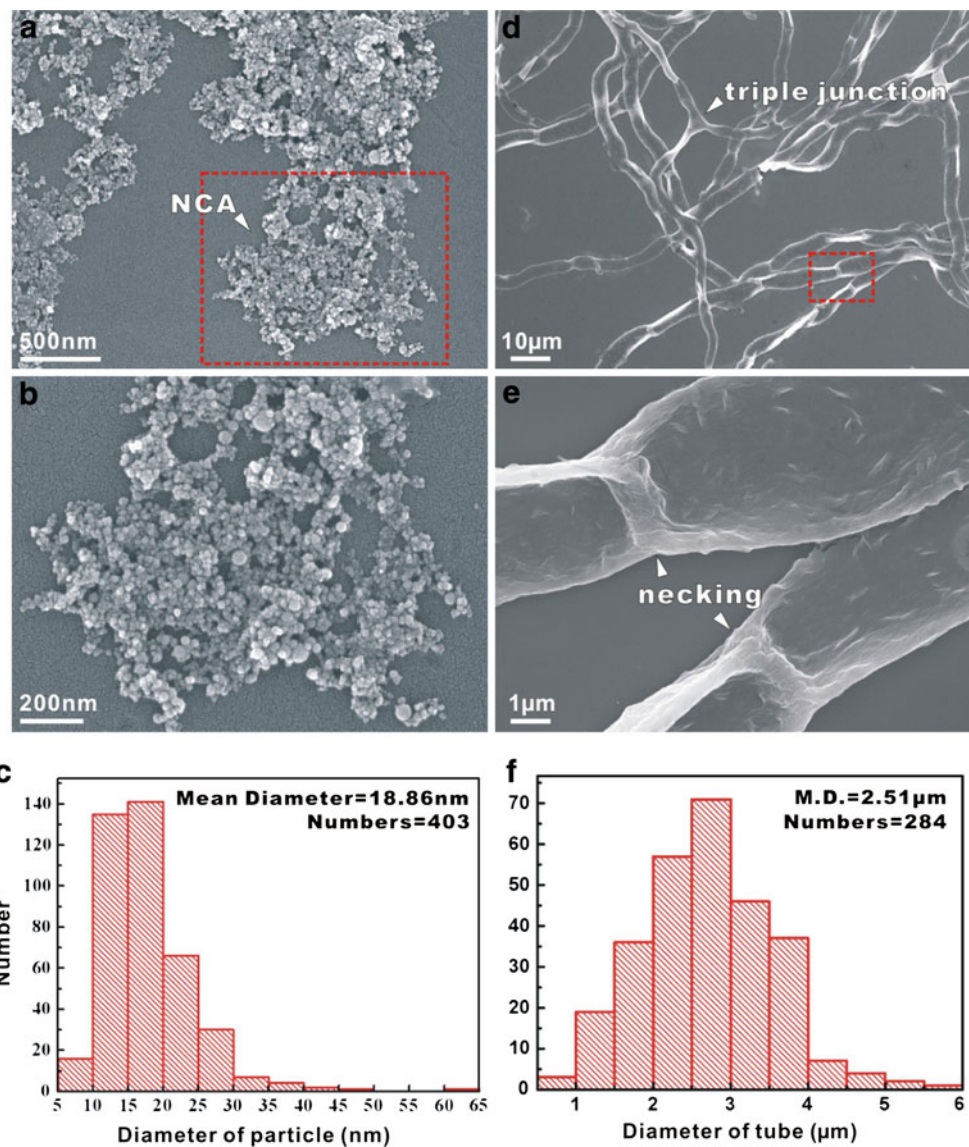
The corresponding SEM observations (Fig. 3) showed further the morphology and size difference between samples 2 and 4. In sample 2, the equiaxed titanium oxide nanoparticles with a mean particle size of ~20 nm were assembled as NCA or in a closely packed manner (Fig. 3a–c). By contrast, the titanium oxide microtubes in sample 4 have a mean diameter as large as 2–3 μm and were entangled or bifurcated leaving necks at the junctions (Fig. 3d–f). In general, the tubes/pipes in samples 3 and 4, i.e. assembled from the nanocondensates fabricated under a relatively high power density, are nearly perfect, unfolded and hierarchical branching, as compiled in Appendix 1.

The compositions of the individual nanoparticles in the less laser power-density activated case, as represented by sample 2, were characterized by STEM to be close to TiO_2 , Ti_5O_9 , and Ti_2O_3 , as compiled in Fig. 4. TEM BFI and lattice image coupled with Fourier transform patterns and point-count EDX analysis of sample 2 further identified the equiaxed nanoparticles of Ti_2O_3 and TiO_2 rutile with {101} twin planes in Fig. 5. The co-existing TiO phase showed corrugated {100} facets and point defects, presumably Ti and/or oxygen vacancies, and occasionally formed bicrystals with (100) tilt boundary due to coalescence over (100) vicinal surfaces (Fig. 6). Dense dioxide nanoparticles, such as $\alpha\text{-PbO}_2$ -type and fluorite-derived type TiO_2 the same as that reported by ref. [17, 18], were occasionally found (not shown). The tubular material assembled from highly activated nanocondensates have corrugated lamellar wall with 0.386 nm interspacing on the average and more or less attached with crystalline nonstoichiometric titania nanoparticles (Fig. 7). The lamellar interspacing is ca. half that of the basal layer (200) interspacing (0.786 nm) of $\text{H}_2\text{Ti}_3\text{O}_7$ [4] implying the former is a disordered precursor of the latter.

EELS and XPS

The background-subtracted Ti L-edge and O K-edge EELS spectra of titanium oxide microtube (sample 4), and the nanocondensates of TiO_2 , Ti_2O_3 , and TiO (sample 2) retrieved from the colloidal solutions as compiled in Fig. 8, showed that the titanium ions are 4+, 3+, and 2+ in valence as for TiO_2 , Ti_2O_3 , and TiO , respectively [19]. The two major L_3 and L_2 edges can be attributed to the spin orbit splitting of the $2p$ core hole for a separation by about 5 eV having the two edges subdivided by the strong crystal-field splitting of Ti^{4+} from the surrounding oxygen atoms in view of the EELS study for anatase, rutile and titania-based nanotubes as well as the calculated spectra using crystal-field multiplet code for Ti^{4+} [20]. The EELS O–K edge exhibited a strong peak due to the Ti 3d and O 2p hybridization which is spitted at 2.5 eV for anatase and 2.75 eV for rutile [20]. By

Fig. 3 **a** SEM secondary electron image (SEI) of titanium oxide nanoparticles assembled as nano-chain aggregate (NCA) in sample 2, **b** magnified from square region in (a) showing equiaxed nanoparticles more or less in coalescence, **c** histogram about the size distribution of the titanium oxide nanoparticles. **d** SEI of titanium oxide microtubes in sample 4 which were entangled, bifurcated at triple junction, and formed necks between the adjoined segments as magnified in (e), **f** histogram about the diameter distribution of the microtubes



contrast, the O–K edge splitting of the present samples is minor for TiO and vague for Ti₂O₃ and microtubes (Fig. 8). Apparently, the Ti L-edge and O K-edge EELS spectra of the titanium oxide microtube are quite different from those of TiO₂ rutile but are similar to those of Ti₂O₃, indicating titanium ions are predominantly in 3+ oxidation state for the microtubes.

The valence state of the nonstoichiometric titania in samples 2 and 4 were further confirmed by XPS Ti 2p_{3/2} and O 1 s peaks coupled with Gaussian fits (Fig. 9) to be predominant 3+ as opposed to 4+ and 2+. Actually, the binding energies around 455.9, 456.7, and 458.5 eV could be identified as TiO, Ti₂O₃, and TiO₂ species. The decomposition of the O 1 s spectrum revealed the binding energies of the individual components to be 530.08 (Ti⁴⁺–O), 531.1 (Ti³⁺–O), 528.3 (Ti²⁺–O), and 532.36 eV

(OH[−]), in agreement with previous work on various titanium oxide phases [21–23].

Vibrational and PL Spectroscopy

The vibrational spectra shed light on the extent of OH[−] signature and the internal stress of the constituent polyhedra of the nonstoichiometric titania. The FTIR spectra of the titanium oxides nanoparticles (sample 2) and microtubes (sample 4) in Fig. 10a showed the latter has much stronger band between 400 and 700 cm^{−1} which can be assigned as Ti–O stretching and Ti–O–Ti bridging stretching after [24] and stronger band near 1057 cm^{−1} which can be attributed to the TiO molecules vibration [25]. The weak bands near 2850 and 2920 cm^{−1} were from EtOH contamination during IR sample preparation for both

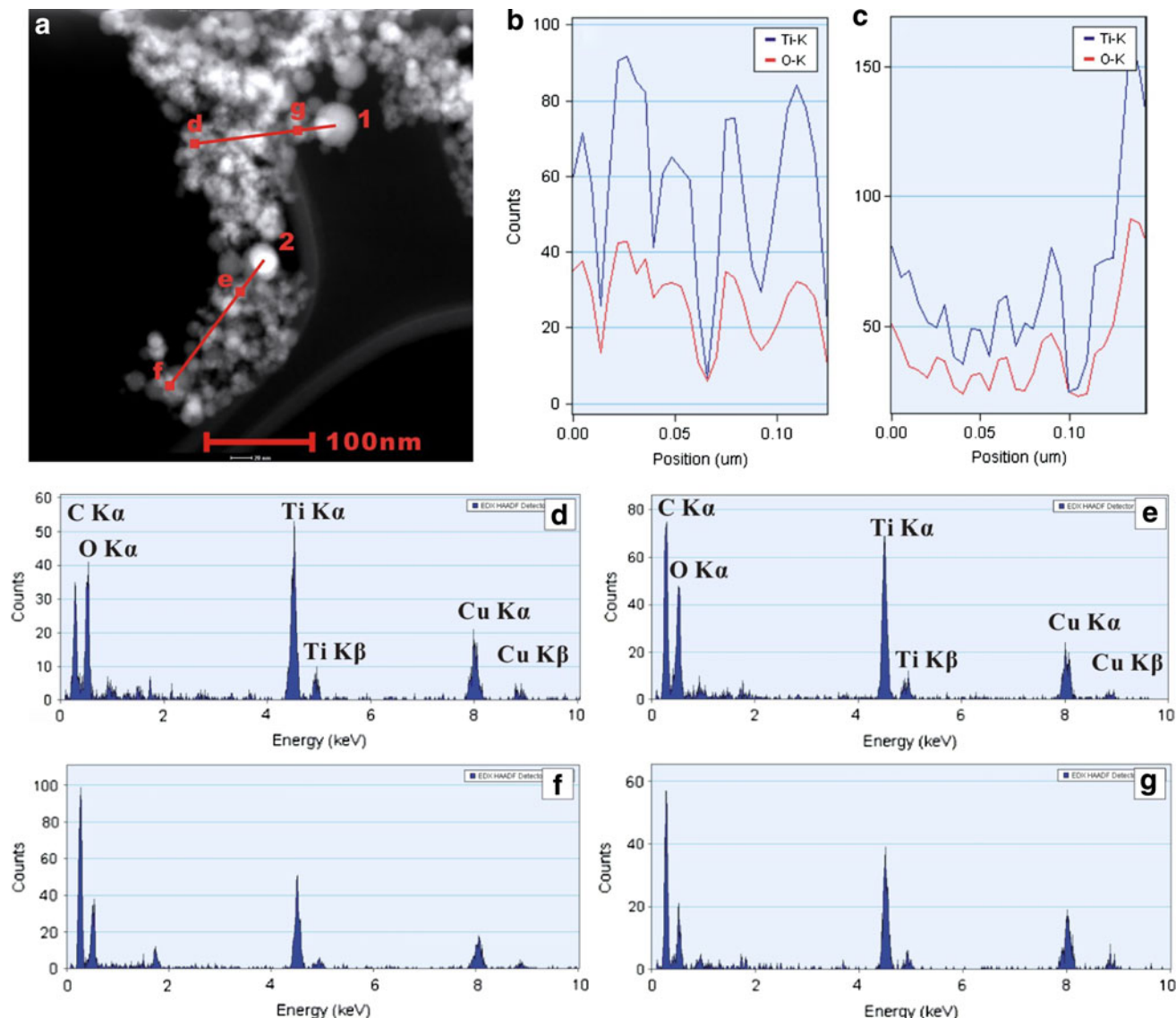


Fig. 4 **a** STEM-HAADF (Z-contrast) image of randomly oriented titanium oxide nanocondensates in sample 2, **b** and **c** EDX scanning profile of lines 1 and 2 showing varied counts of Ti and O, **d–g** point count analysis at point **d–g** as labeled in the image for titanium oxide

nanocondensates with decreasing O/Ti ratio. The Cu and C peaks are from supporting copper grids overlaid with a carbon-coated collodion film

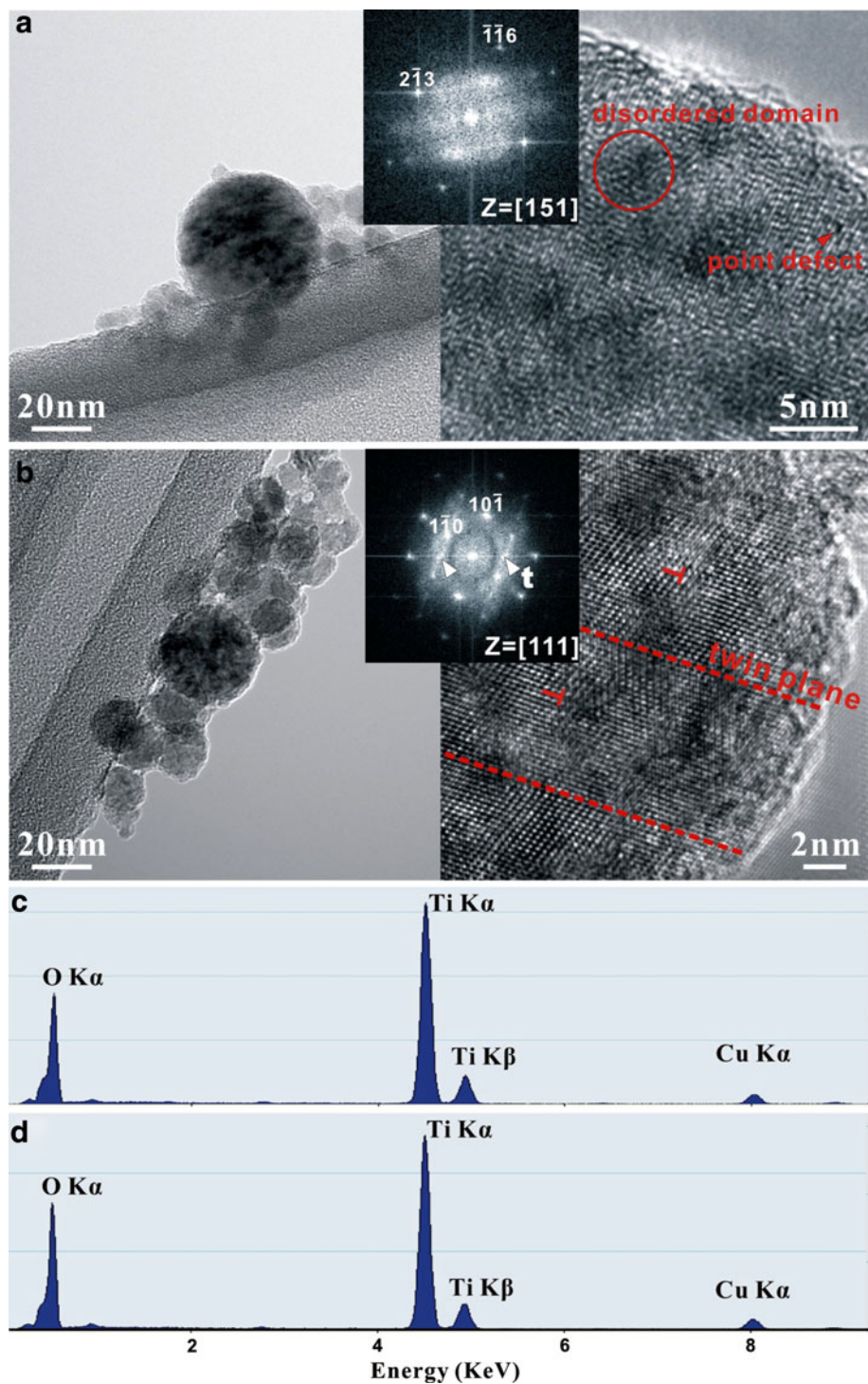
cases. The extent of Ti^{3+} –O stretching below 700 cm^{-1} [26] cannot be differentiated because of the common broad band around 600 cm^{-1} for the present two cases.

The OH^- signature of the nanoparticles and microtubes were testified by the IR band near 3430 cm^{-1} analogous to the fully hydroxylated rutile surface having three distinct absorption bands around 3655 , 3530 , and 3400 cm^{-1} [27]. The hydroxyl groups were likely associated with a number of different surface sites of the nonstoichiometric titania in the present case to cause various interactions, such as hydrogen bonding between surface OH groups and molecular water with bending vibration near 1640 and 1726 cm^{-1} after the assignment of ref. [27], and hence a

broad IR band analogous to the case of hydroxyl groups linkage to TiO_2 rutile and anatase [28]. The microtubes were much more OH-signified than the nanoparticles upon dwelling in water for a week. The combined results of XRD and Raman shifts indicated that the protonated microtube is structurally different from titanium hydrate, such as $\text{H}_2\text{Ti}_3\text{O}_7$ [6, 7].

The Raman shifts of the nanoparticles in sample 2 are mainly 614 (A_{1g}), 443 (E_g), 248 (due to second order phonon), and 144 cm^{-1} (B_{1g}) with the assigned modes of TiO_6 octahedra in parenthesis (Fig. 10b) after the assignment of rutile by ref. [29] and [30]. These Raman shifts change to 606 , 416 , 264 , and 414 cm^{-1} , respectively, for

Fig. 5 TEM BFI (left) and lattice image (right) coupled with Fourier transform inset for relatively large (>30 nm) and spherical titanium oxide nanocondensates having various stoichiometries in sample 2 which was fabricated by PLAL under FR-mode and then dwelling in water for 1 week: **a** Ti_2O_3 with point defects and disordered domains as viewed in [151] zone axis, **b** TiO_2 rutile in [111] zone axis showing {101} twin planes and dislocations half plane parallel to $(10\bar{1})$, **c** and **d** Point-count EDX spectrum of the Ti_2O_3 and TiO_2 particles in (a) and (b), respectively, showing varied Ti and O counts (40.3 at.% Ti and 59.7 at% O for the former, whereas 34.3 at.% Ti and 65.6 at% O for the latter) with Cu counts from supporting copper grids

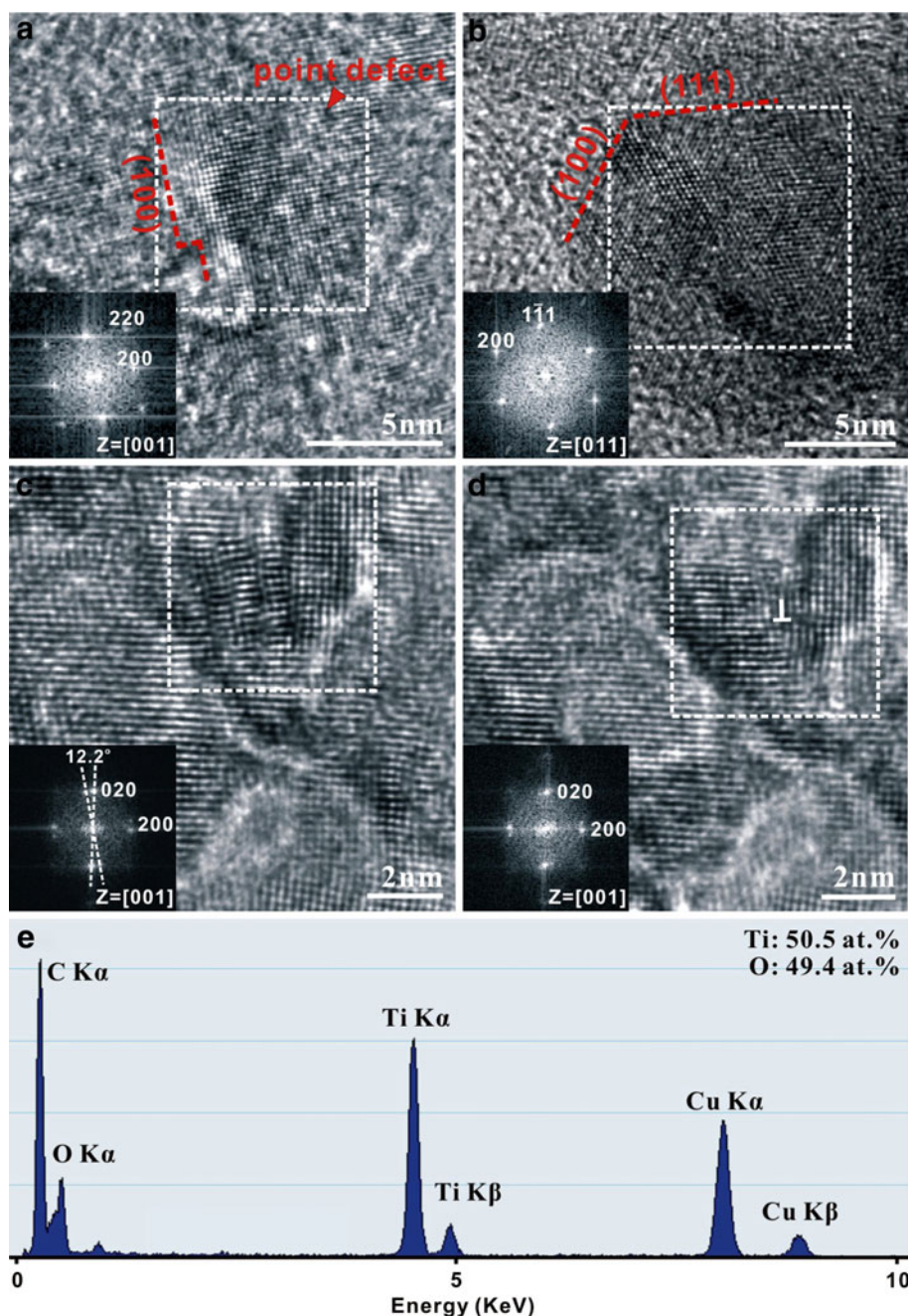


the microtubes in sample 4. This indicates that the extent of TiO_6 distortion in terms of internal stress is different, according to pressure dependence of TiO_6 Raman shifts as discussed in Sect. 4. The Ti ion charges/oxygen vacancies are also considerably different in the two cases to change the vibration/stretching behavior as indicated by the presence of Ti_2O_3 with characteristic band at 344 cm^{-1} due to Ti^{3+} occupancy in octahedral site [31, 32] for sample 2 but

not for sample 4, although monoxide TiO is not Raman active [33] to support this point.

The PL spectra of samples 2 and 4 (Fig. 11) showed that the luminescence of the present nonstoichiometric titania nanoparticles and microtubes covers a rather broad wavelength from 400 to 700 nm with individual peaks much broader than the case of alkaline stabilized titanate nanotubes with TiO_6 octahedral units [34]. The PL bands at 2.84

Fig. 6 Lattice images with inset Fourier transform from square region for the TiO nanocondensates less than 15 nm in size in sample 2 which was fabricated by PLAL under FR-mode and then dwelling in water for 1 week: **a** single crystal with corrugated {100} facets and point defects presumably Ti and/or oxygen vacancies indicated by a red arrow), **b** another single crystal in [011] zone axis showing {100} and {111} facets, **c** bicrystals with (100) tilt boundary due to coalescence over (100) vicinal surfaces (off by 12.2 degree) viewed edge on in [001] zone axis, **d** the tilt boundary became healed with a relic dislocation (denoted as T) after electron irradiation for 30 s, **e** point-count EDX spectrum of the TiO nanoparticle in (**a**) showing Ti and O counts (50.5 at% of Ti and 49.4 at% of O), with Cu and C peaks from supporting copper grids overlaid with a carbon-coated collodion film



and 2.74 eV were probably originated from the self-trapped excitons localized on the TiO_6 octahedra [35]. These types of trapped sites were found below the conduction band edge due to the conduction band splitting [35]. The bands at 2.53 and 2.02 eV were attributed to oxygen vacancies [22]. The 2.53 eV vacancy level, which corresponds to 1.05 eV below conduction band for a band gap of 3.6 eV, has been attributed to Ti^{4+} ions adjacent to oxygen vacancies by the intragap surface states. This deep electron trap has been confirmed using femtosecond photogenerated charge dynamics in TiO_2 nanoclusters [36]. The band at 2.47 eV could be attributed to the TiO_6 octahedra as the

basic structural unit analogous to the titanate nanotube [34]. The band at 2.31 eV is assigned to Ti_2O_3 [37]. The band at 2.16 eV can be assigned to the shallow trap level related to oxygen vacancies on the surface of TiO_2 nanotube. The PL emission identified with oxygen vacancies might have occurred with photogenerated conduction band electrons trapped by ionized oxygen vacancy levels in TiO_2 nanotube and subsequently recombined with the holes in the valence band [35].

Based on the above vibration and PL spectroscopic analyses, the TiO_6 octahedral are likely the common units for the present titania nanoparticle/microtubes and the

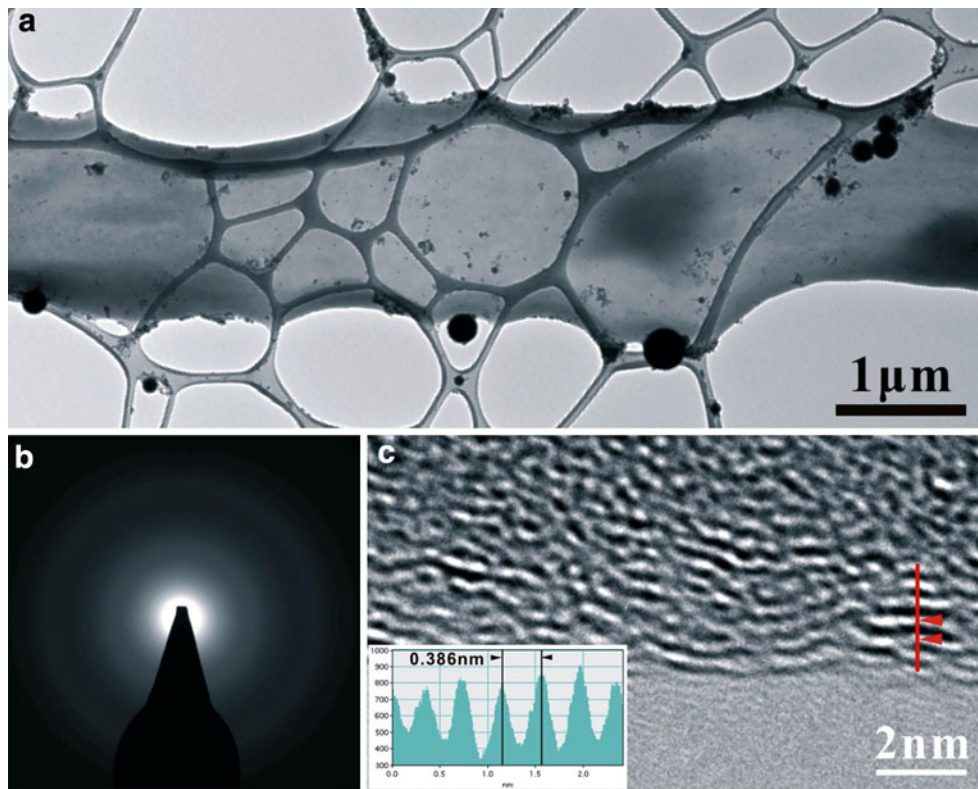


Fig. 7 **a** and **b** TEM BFI and corresponding SAED pattern of the amorphous titanium oxide microtube (i.e. sample 4 in Table 1) on a carbon lacey support film, **c** lattice image with the intensity profile along the trace (*red line*, orthogonal to the elongate direction of the

tube) inset showing the corrugated lamellar wall are 0.386 nm interspaced on the average ca. half that of the $\text{H}_2\text{Ti}_3\text{O}_7$ (0.786 nm) implying a close structure linkage (cf. text)

crystalline titanium hydrate nanotubes, such as $\text{H}_2\text{Ti}_3\text{O}_7$ with long range ordering in the basal layer [6, 7] or other stoichiometries with controversial structures [8–10].

Discussion

Effect of PLAL Parameter on the Phase Selection of Titanium Oxide

The PLAL by free run with a relatively low power density caused more TiO , Ti_2O_3 , and TiO_2 than the amorphous phase (cf. Table 1). By contrast, Q-switch mode with a higher power density caused more oxidized crystallites, i.e. TiO_2 rather than TiO and Ti_2O_3 as in the case of sample 4, besides the predominant amorphous lamellar phase which further assembled and rolled up as microtubes upon dwelling in water. Apparently, PLAL under a higher power density would cause more thorough oxidation of the nanocondensates on the one hand and the amorphous phase on the other hand. In fact, by rapid reactive quenching with water in the liquid-plasma interface, the ablated species can be readily oxidized [38]. As for phase amorphization by a dynamic condensation and very rapid cooling process, it

has been demonstrated by the PLA synthesis of amorphous Al_2O_3 nanocondensates [39]. The cooling rate in the similar PLA process was estimated to be close to 10^9 K/s for 10-nm-sized Al_2O_3 [39] as well as $\alpha\text{-PbO}_2$ type TiO_2 nanocondensates [17], 4 orders of magnitude higher than that required to quench an amorphous state for oxides [40]. The PLAL process is expected to have an even higher cooling rate under the influence of water rather than air cooling, to quench the present titania nanocondensates as amorphous state under an additional factor of a rather large extent of nonstoichiometry and associated defect clusters as addressed in next section.

The application of pressure to certain crystalline materials, i.e. so-called pressure induced amorphization, can cause them to become amorphous under certain conditions [41]. An anatase-amorphous transition regime was also reported to occur for TiO_2 of very fine crystallite size upon static compression at room temperature using the diamond anvil cell technique [42]. Shock-wave loading and liquid confinement typical for a PLAL process [43] would also cause the already crystallized nonstoichiometric titania to become amorphous. In this connection, PLAL of TiO_2 single crystal and Ti plate targets under the wavelength of 355 nm and maximum laser pulse energy 160 mJ/pulse in

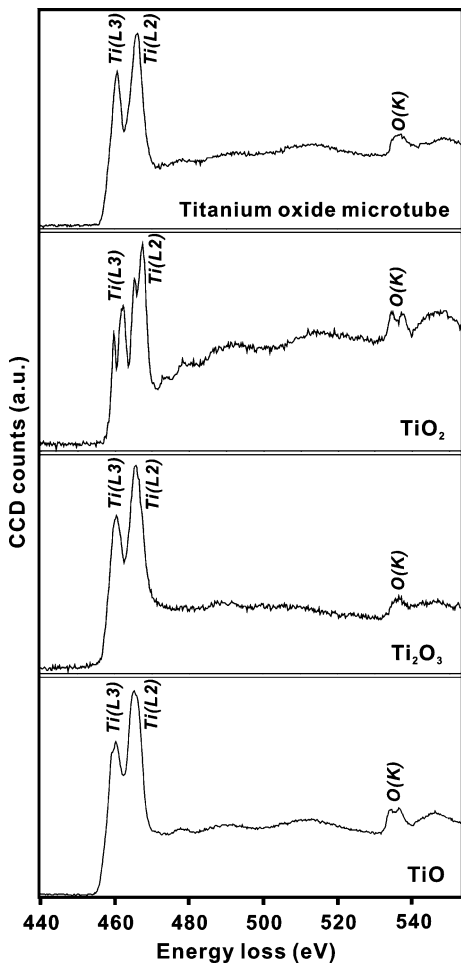


Fig. 8 Ti L-edge and O K-edge EELS spectra of titanium oxide microtube (sample 4), and the nanocondensates of TiO_2 , Ti_2O_3 , and TiO (sample 2) retrieved from the colloidal solutions

de-ionized water was reported to cause mostly amorphous phase [38]. The amorphous lamellae appeared to be formed by a relatively high power density in the present PLAL process and then assembled and rolled up as microtubes upon subsequent dwelling in water. It is not clear, however, whether the amorphous lamellae are in high-density amorphous state [44].

Stress States of the Nanocondensates and Microtubes

The TiO_2 rutile nanoparticles in samples 1 to 4 have a significant internal stress up to 4–5 GPa for the lattice (Table 1) based on SAED lattice parameters and the Birch–Murnaghan equation of state of the rutile with relevant bulk modulus and its pressure derivative [45].

The Raman shifts provide another estimation of the internal stress in terms of the TiO_6 polyhedra shared by the TiO , Ti_2O_3 , and TiO_2 and amorphous lamellar phase in the samples. Regarding this approach, the pressure dependence of Raman shifts has been studied for anatase [42] and rutile-

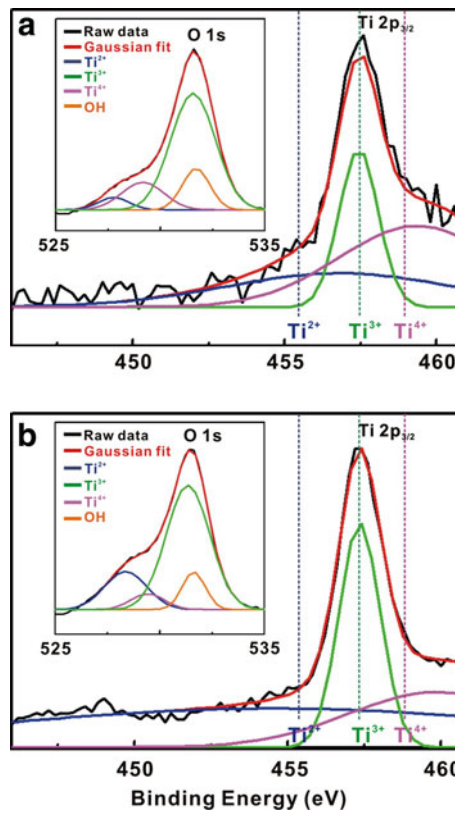


Fig. 9 **a** and **b** XPS spectra of OH-signified titanium oxide nanoparticles (sample 2 in Table 1) and microtubes (sample 4 in Table 1), respectively, showing O 1s and Ti 2p_{3/2} signals with Gaussian fits showing a predominant Ti^{3+} as opposed to Ti^{4+} and Ti^{2+} in the presence of OH species (cf. text). Note the Ti^{2+} content is significantly higher in sample 2 than sample 4 in accord with a lower minimum band gap for the former

type TiO_2 [46]. The major Raman modes ($E_{g(1)}$, $B_{1g(1)}$, $A_{1g} + B_{1g}$, $E_{g(3)}$) of anatase nanocrystals are all well represented by linear increases in Raman shift with pressure up to 41 GPa [42]. (The Raman modes E_g and A_{1g} of the synthetic rutile-type TiO_2 single crystal also have a higher wave number under an applied pressure up to 35 GPa [46]). Using both calibration curves, the TiO_6 polyhedra of the present TiO_{1-x} , $\text{Ti}_2\text{O}_3 - x$, and $\text{TiO}_2 - x$ and amorphous lamellar have quite different stress state from that of the rutile lattice based on its lattice parameters. The internal compressive stress for the TiO_6 polyhedra of the TiO , Ti_2O_3 , and TiO_2 nanocondensates in sample 2 is indicated by its A_{1g} mode but not E_g mode being at a higher wave number than the reported ambient value of anatase (513 cm^{-1}) [40] or rutile (608 cm^{-1}) [29]. In other words, there is a significant distortion of the polyhedra in the present nonstoichiometric titania phases due to the combined effects of quenching a dense state and varied stoichiometry and protonation. The TiO_6 polyhedra of the microtubes in sample 4 were quite relaxed based on the A_{1g} and E_g modes being at a much lower wave number (606 , 416 cm^{-1}) than the titanium oxide

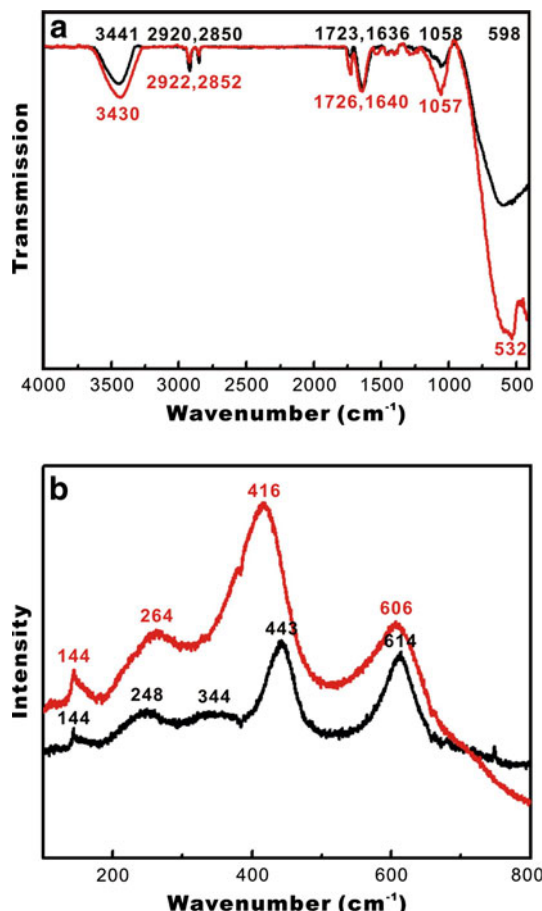


Fig. 10 **a** FTIR spectra of the titanium oxide nanoparticles (black line, sample 2 in Table 1) and microtubes (red line, sample 4 in Table 1) with significant OH⁻ signature as indicated by free OH groups around 3400 cm⁻¹ and molecular water around 1720 and 1630 cm⁻¹ (cf. text). Note the microtubes were more OH-signified than the nanoparticles but did not change into crystalline titanium hydrates (cf. text) upon dwelling in water for a week. **b** Raman spectra of the titanium oxide nanoparticles (black line, sample 2 in Table 1) and microtubes (red line, sample 4 in Table 1) showing the bands of rutile at 614, 443, 248, and 144 cm⁻¹ in sample 2 change to 606, 416, 264, and 414 cm⁻¹, respectively, and the band at 344 cm⁻¹ for Ti₂O₃ in sample 2 is ambiguous for sample 4. The monoxide TiO cannot be detected since it is not Raman active (cf. text)

nanocondensates in sample 2 (614, 443 cm⁻¹). This indicates that the TiO₆ polyhedra in the amorphous lamellae were relaxed when the lamellae were rolled into microtubes. It should be noted that size, nonstoichiometry, and temperature would also affect the vibration mechanism of the TiO₆ polyhedra, as indicated by previous Raman shifts study of rutile [5, 29, 30].

Defect Chemistry due to Hydrolysis and Polymerization of Ti–O–H

The present nanocondensates have a rather high Ti³⁺/Ti²⁺ and Ti³⁺/Ti⁴⁺ atomic ratio and OH⁻ signature according to XPS

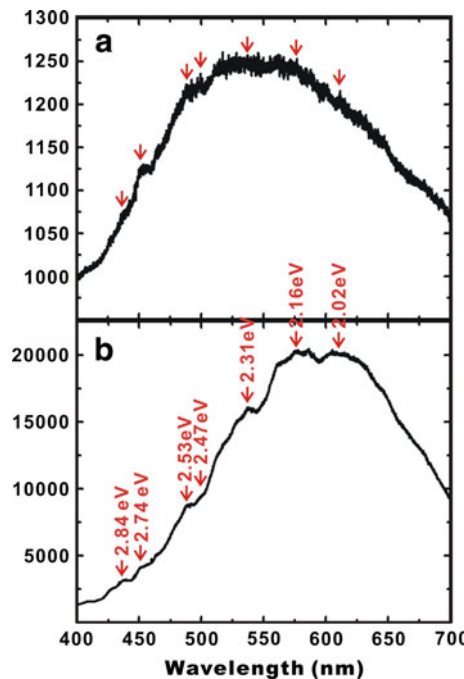
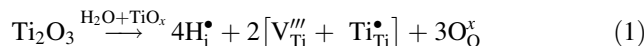
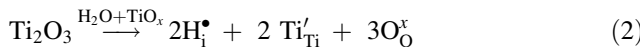


Fig. 11 Photo-luminescence spectra of titanium oxide **a** nanoparticles (sample 2) and **b** microtubes (sample 4), the latter having an order-of-magnitude higher emission band from 400 to 700 nm. There are more distinct peaks at specified eVs for the microtubes in **(b)** in comparison with the nanoparticles in **(a)**. This is due to a larger amount of microtubes with predominant amorphous lamellar wall rather than crystalline TiO, Ti₂O₃, and TiO₂ (cf. text)

and FTIR results, respectively. In other words, the Ti³⁺ and the dopant Ti²⁺, Ti⁴⁺, and H⁺ ion species were co-incorporated in the TiO, Ti₂O₃, and TiO₂ and amorphous lamellar when fabricated by PLAL. Under such a complicated case, charge-compensating defect clusters [V_{Ti}''' + Ti_{Ti}]⁺ in association with the interstitial proton in the predominant Ti₂O₃ as indicated by XPS would occur through the following equation in Kröger-Vink notation [47]:



Here, H_i⁺ signifies single positively charged hydrogen in the interstitial octahedral and/or tetrahedral sites; Ti_{Ti}⁺ dominating single positively charged titanium at titanium sites and V_{Ti}''' triple negatively charged titanium vacancies in the crystal lattice. In such a defect chemistry scheme, the Ti⁴⁺ (effective ionic radii, 0.0605 nm) would replace a larger sized Ti³⁺ (0.067 nm) in CN 6 [48], for the volume compensation of interstitial protons. It is also possible that the volume-compensating effect, due to the undersized Ti⁴⁺ dopant in the Ti³⁺ site, forced Ti_{Ti}⁺ to enter the interstitial tetrahedral site, i.e. Ti_{Ti}⁺, and hence more charge-compensating cation vacancies. Alternatively, Ti²⁺ may act as dopant by substituting Ti³⁺ and hence charge compensates the interstitial protons through the following equation:



The oxygen vacancies and titanium interstitials were suggested to be the dominant defects in TiO_2 rutile under low oxygen atmosphere [49] or doped with cation with lower valence such as Zn^{2+} [50]. The titanium vacancies are however favored in the present Ti_2O_3 to charge compensate the proton dopant. In fact, Ti_2O_3 allows a considerable extent of nonstoichiometry with O/Ti ratio ranging from 1.48 to 1.51 in the Ti–O binary at temperatures [49]. The incorporation of proton during PLAL is expected to cause an even higher O/Ti ratio by introducing more titanium vacancies through Eq. 1.

The defect clustering of Ti^{2+} , Ti^{4+} , and H^+ co-doped Ti_2O_3 through Eqs. 1 and 2 may be effective as soon as the oxidation by forming Ti–O–H linkage, typical in a hydrothermal process [51], caused considerable polymerization and various defect clusters in the crystals as observed by TEM. The hydrolysis and polymerization process to form specific Ti–O–H species is quite effective so that the sedimentation of the nanoparticles is much faster than Au nanoparticles via the same PLAL process [12]. Aside from the detailed defect clustering scheme, the co-existence of Ti^{2+} , Ti^{3+} , Ti^{4+} , and H^+ ions and charge/volume-compensating defects in the present nonstoichiometric titanium oxides would account for the Raman shift of rutile Eg band in view of the Ti/O ratio dependence of Raman shift for nanophase TiO_2 rutile and anatase [52].

Rolling and Tubing of the Assembled Nanocondensates

The formation of tubes/pipes in samples 3 and 4 versus NCA or closely packed manner in samples 1 and 2 can be attributed to different growth mechanisms. The former case is analogous to the Au clusters being assembled as lamellae and then rolled up as Au micro- and nano-tubes [12]. To roll up a planar layer, it requires either caps as for carbon nanotubes with single or multiple walls [53] or intrinsic structural anisotropy as for clay minerals chrysotile [54]. Only intrinsic structural anisotropy is considered here for the protonated microtubes. We suggest that the amorphous titania lamellae stabilized via oxidation in the PLAL process were water/air interface-mediated at the water level and bubbles to become asymmetric on the opposite sides, i.e. more H^+ signified on the water side to exert a strain field for rolling up upon dwelling in water.

The $\text{H}_2\text{Ti}_3\text{O}_7$ nanotube with monoclinic structure (space group $C2/m$) based on ab initio calculations and TEM examinations has been synthesized by treating TiO_2 powders in concentrated NaOH in aqueous solution and then individual trititanate layers are peeled off from the plates and scroll up into nanotubes [6, 7, 55]. It was found that

surface tension due to an asymmetry related to H deficiency in the surface layers of the plates is the principle driving force of the cleavage, and the dimension of the nanotubes is controlled by this surface tension together with interlayer coupling energy and Coulomb force [55]. However, $\text{H}_2\text{Ti}_3\text{O}_7$ was not formed in samples 2 and 4 based on the combined XRD, FTIR, and Raman results. The reasons of forming protonated amorphous titanate microtubes with multiple lamellar wall rather than $\text{H}_2\text{Ti}_3\text{O}_7$ nanotube in the present PLAL process could be the following. First, the present samples were synthesized under water rather than high concentration of Na^+ cations and strongly basic conditions for alkali-treated processes that are essential in the synthesis of the titanium hydrate nanotubes [6]. Second, dynamic high pressure–temperature conditions and very rapid heating/cooling rate via the present PLAL process may favor amorphous lamellae rather than $\text{H}_2\text{Ti}_3\text{O}_7$ which typically has corrugated ribbons of edge-shared TiO_6 octahedrons via a thermal equilibrium synthesis route [7].

Conclusions

Titania nanotubes have been synthesized and morphologically tailored by acids and electrolytes for potential bioactivity applications [56]. The nonstoichiometric titania nanoparticles and microtubes as fabricated by PLAL here may also have potential optoelectronic and catalytic applications in UV–visible range as indicated by the band gap and the broad photoluminescence from 400 to 700 nm due to the incorporation of Ti ions with various charges and hence varied extent of crystal field stabilization energy under the influence of Jahn–Teller effect [57]. (The Ti^{3+} ion therefore prefers to occupy octahedral rather than tetrahedral site with the so-called octahedral site preference energy of -28.8 kJ/mole [57].) It is of interest to explore in the future whether the oxygen deficiency in such PLAL products can be further increased to cause strong absorbance and photoluminescence as the case of titanic acid nanotubes [58]. Finally, the titanium hydrates being not favored under highly activated dynamic conditions by the present PLAL route sheds light on the Ti charge and phase behavior of titania–water binary in natural shock occurrence.

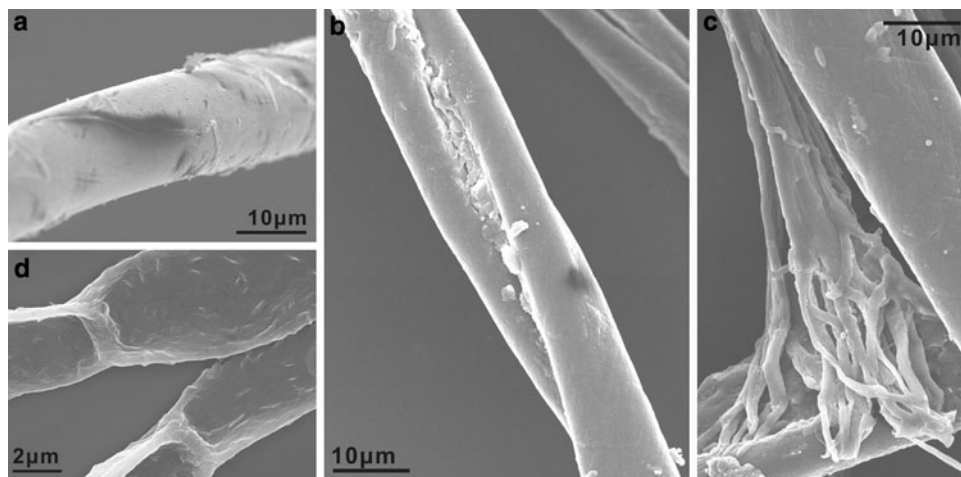
Acknowledgments We thank Miss S.Y. Shih for the help on XPS analysis. This research was supported by Center for Nanoscience and Nanotechnology at NSYSU and partly by National Science Council, Taiwan, ROC.

Open Access This article is distributed under the terms of the Creative Commons Attribution Noncommercial License which permits any noncommercial use, distribution, and reproduction in any medium, provided the original author(s) and source are credited.

Appendix 1

See Fig. 12.

Fig. 12 SEM secondary electron image (SEI) of tubular TiO_x assembled from the nanocondensates fabricated by PLAL under Q-switch mode (i.e. sample 3 (*panels a, b, and c*) and 4 (*panel d*) in Table 1) for various morphologies: **a** nearly perfect pipe, **b** unfolded pipe, **c** hierarchical branches within the pipe, **d** necking of the connected pipes (the same as Fig. 2e)



References

1. Z. Pan, Z. Dai, Z. Wang, *Science* **291**, 1947 (2001)
2. Z. Wang, X.Y. Ma, J.W. Song, J.H. Yao, *Nano-Micro Lett.* **1**, 45 (2009)
3. A.L. Linsebigler, G. Lu, J.T. Yates, *Chem. Rev.* **95**, 735 (1995)
4. H. Cheng, J. Ma, Z. Zhao, L. Qi, *Chem. Mater.* **7**, 663 (1995)
5. T. Kasuga, M. Hiramatsu, A. Hosono, T. Sekino, K. Niihara, *Adv. Mater.* **11**, 1307 (1999)
6. Q. Chen, G.H. Du, S. Zhang, L.M. Peng, *Acta Cryst. B* **58**, 587 (2002)
7. Q. Chen, W. Zhou, G. Du, L.M. Peng, *Adv. Mater.* **14**, 1208 (2002)
8. R. Ma, K. Fukuda, T. Sasaki, M. Osada, Y. Bando, *J. Phys. Chem. B* **109**, 6210 (2005). and references cited therein
9. C.C. Tsai, H. Teng, *Chem. Mater.* **18**, 367 (2006). and references cited therein
10. J.N. Nian, H. Teng, *J. Phys. Chem. B* **110**, 4193 (2006). and references cited therein
11. N. Sano, H. Wang, M. Chhowalla, I. Alexandrou, G.A.J. Amaralunga, *Nature* **414**, 506 (2001)
12. C.N. Huang, S.Y. Chen, Y. Zheng, P. Shen, *Nanoscale Res. Lett.* **4**, 1064 (2009)
13. M.Y. Kuo, C.L. Chen, H.C. Yang, C.Y. Hua, P. Shen, *Phys. Rev. B* **71**, 125405 (2005)
14. M.Y. Kuo, C.L. Chen, C.Y. Hua, H.C. Yang, P. Shen, *J. Phys. Chem. B* **109**, 8693 (2005)
15. M. Iwasaki, M. Hara, H. Kawada, H. Tada, S. Ito, *J. Colloid Interface Sci.* **224**, 202 (2000)
16. J.C. Yu, J. Yu, W. Ho, Z. Jiang, L. Zhang, *Chem. Mater.* **14**, 3808 (2002)
17. S.Y. Chen, P. Shen, *Phys. Rev. Lett.* **89**, 096106 (2002)
18. S.Y. Chen, P. Shen, *Jap. J. Appl. Phys.* **43**, 1519 (2004)
19. B. Cao, K. Suenaga, T. Okazaki, H. Shinohara, *J. Phys. Chem. B* **106**, 9295 (2002)
20. A. Gloter, C. Ewels, P. Umek, D. Arcon, C. Colliex, *Phys. Rev. B* **80**, 035413 (2009)
21. A.F. Carley, G. Spoto, P.R. Chalker, J.C. Riviere, M.W. Roberts, *J. Chem. Soc. Faraday Trans.* **83**, 351 (1987)
22. J. Pouilleau, D. Devilliers, H. Groult, P. Marcus, *J. Mater. Sci.* **32**, 5645 (1998)
23. P.M. Kumar, S. Badrinarayanan, M. Sastry, *Thin Solid Film* **358**, 122 (2000)
24. J.G. Yu, H.G. Yu, B. Cheng, X.J. Zhao, J.C. Yu, W.K. Ho, *J. Phys. Chem. B* **107**, 13871 (2003)
25. M. Zhou, L. Zhang, J. Dong, Q. Qin, *J. Am. Chem. Soc.* **122**, 10680 (2000)
26. M. Manickam, P. Singh, T.B. Issa, S. Thurgate, *J. Appl. Electrochem.* **36**, 599 (2006)
27. Y. Suda, T. Morimoto, M. Nagao, *Langmuir* **3**, 99 (1987)
28. B. Erdem, R.A. Hunsicker, G.W. Simmons, D. Sodul, V.L. Dimonie, M.S. El-Aasser, *Langmuir* **17**, 2664 (2001)
29. S.P.S. Porto, P.A. Fleury, T.C. Damen, *Phys. Rev. B* **154**, 522 (1967)
30. R.J. Betsch, H.L. Park, W.B. White, *Mater. Res. Bull.* **26**, 613 (1991)
31. A.P. del Pino, P.S. Serra, J.L. Morenza, *Appl. Surf. Sci.* **197-198**, 887 (2002)
32. P. Kern, Y. Müller, J. Patscheider, J. Michler, *J. Phys. Chem. B* **110**, 23660 (2006)
33. A.P. del Pino, P.S. Serra, J.L. Morenza, *Surf. Coat. Technol.* **187**, 106 (2004)
34. K. Yoshida, L. Miao, N. Tanaka, S. Tanemura, *Nanotechnology* **20**, 405709 (2009)
35. S.E. John, S.K. Mohapatra, M. Misra, *Langmuir* **25**, 8240 (2009)
36. D.P. Colombo Jr., K.A. Roussel, J. Sach, D.E. Skinner, J.J. Cavalieri, R.W. Bowman, *Chem. Phys. Lett.* **232**, 207 (1995)
37. S. Komuro, T. Katsumata, H. Kokai, T. Morikawa, X. Zhao, *Appl. Phys. Lett.* **81**, 4733 (2002)
38. T. Sasaki, C. Liang, W.T. Nichols, Y. Shimizu, N. Koshizaki, *Appl. Phys. A* **79**, 1489 (2004)
39. C. Pan, P. Shen, S.Y. Chen, *J. Crystal Growth* **299**, 393 (2007)
40. C.G. Levi, V. Jayaram, J.J. Valencia, R.J. Mehrabian, *J. Mater. Res.* **3**, 969 (1988)
41. S.R. Elliott, *Physics of Amorphous Materials*, 2nd edn. (Longman Sci. Tech., Essex, 1990)
42. V. Swamy, A. Kuznetsov, L.S. Dubrovinsky, R.A. Caruso, D.G. Shechukin, B.C. Muddle, *Phys. Rev. B* **71**, 184302 (2005)
43. G.W. Yang, *Prog. Mater. Sci.* **52**, 648 (2007)
44. V. Swamy, A. Kuznetsov, L.S. Dubrovinsky, P.F. McMillan, V.B. Prakapenka, G. Shen, B.C. Muddle, *Phys. Rev. Lett.* **96**, 135702 (2006)

45. J.S. Olsen, L. Gerward, J.Z. Jiang, *J. Phys. Chem. Solid* **60**, 229 (1999)
46. W.S. Xiao, Z. Hong, D.Y. Tan, K.N. Weng, Y.C. Li, C.J. Luo, L. Jing, H.S. Xie, *Spectros. Spectral Anal.* **27**, 1340 (2007)
47. F.A. Kröger, H.J. Vink, *Solid State Phys.* **3**, 307 (1956)
48. R.D. Shannon, *Acta Cryst. A* **32**, 751 (1976)
49. O.T. SØrensen (ed.), *Non-Stoichiometric Oxides* (Academic Press, New York, 1981). and literatures cited therein
50. T. Chen, P. Shen, *J. Phys. Chem. C* **113**, 328 (2009)
51. J. Yang, S. Mei, J.M.F. Ferreira, P. Norby, S. Quaresmâ, *J. Colloid Interface Sci.* **283**, 102 (2005)
52. J.C. Parker, R.W. Siegel, *Appl. Phys. Lett.* **57**, 943 (1990)
53. P.J.F. Harris, *Carbon Nanotubes and Related Structures—New Materials for the Twenty-first Century* (Cambridge University Press, Cambridge, 1999)
54. D.R. Veblen, P.R. Buseck, *Science* **206**, 1398 (1979)
55. S. Zhang, L.M. Peng, Q. Chen, G.H. Du, G. Dawson, W.Z. Zhou, *Phys. Rev. Lett.* **91**, 256103 (2003)
56. D. Gong, C.A. Grimes, O.K. Varghese, W. Hu, R.S. Singh, Z. Chen, E.C. Dickey, *J. Mater. Res.* **16**, 3331 (2001)
57. R.G. Burns, *Mineralogical Applications of Crystal Field Theory* (Cambridge University Press, Cambridge, 1993)
58. L. Qian, Z. Jin, J. Zhang, Y.B. Huang, Z.J. Zhang, Z.L. Du, *Appl. Phys. A* **80**, 1801 (2005)